

A DEEP CHANDRA OBSERVATION OF ABELL 4059: A NEW FACE TO “RADIO-MODE” AGN FEEDBACK?

CHRISTOPHER S. REYNOLDS¹, ELYSE A. CASPER,^{1,2} AND SEBASTIAN HEINZ³

Accepted for the Astrophysical Journal

ABSTRACT

A deep Chandra observation of the cooling core cluster Abell 4059 (A4059) is presented. Previous studies have found two X-ray cavities in the central regions of A4059 together with a ridge of X-ray emission 20 kpc south-west of the cluster center. These features are clearly related to the radio galaxy PKS 2354–35 which resides in the cD galaxy. Our new data confirm these previous findings and strengthen previous suggestions that the south-western ridge is colder and denser than, but in approximate pressure equilibrium with, the surrounding ICM atmosphere. In addition, we find evidence for a weak shock that wraps around the north and east sides of the cavity structure. Our data allow us to map the 2-dimensional distribution of metals in the ICM of A 4059 for the first time. We find that the SW ridge possesses an anomalously high (super-solar) metallicity. The unusual morphology, temperature structure and metal distribution all point to significant asymmetry in the ICM atmosphere prior to the onset of radio-galaxy activity. Motivated by the very high metallicity of the SW ridge, we hypothesize that the ICM asymmetry was caused by the extremely rapid stripping of metal enriched gas from a starburst galaxy that plunged through the core of A4059. Furthermore, we suggest that the onset of powerful radio-galaxy activity in the cD galaxy may have been initiated by this starburst/stripping event, either via the tidal-shocking of cold gas native to the cD galaxy, or the accretion of cold gas that had been stripped from the starburst galaxy.

Subject headings: galaxies: abundances — galaxies: clusters: individual (A4059) — galaxies: individual (PKS 2354-350) — galaxies: jets — X-rays: galaxies: clusters

1. INTRODUCTION

In the core regions of galaxy clusters, X-ray observations directly reveal the radiative cooling of the intra-cluster medium (ICM). In most relaxed clusters, the radiative cooling time is measured to be substantially less than the Hubble time (see Peterson & Fabian (2006)). In the absence of a balancing heat source, this cooling would result in a slow flow of matter inwards towards the center of the cluster, a cooling flow (Cowie & Binney 1977; Fabian & Nulsen 1977; Fabian 1994), and a growing central mass of cooled gas. The absence of signatures of this cold gas at non-X-ray wavelengths leads to the cooling flow problem. More recently, high-resolution X-ray spectroscopy with *XMM-Newton* has shown an almost complete lack of gas below a temperature of $T_{\text{vir}}/3$, where T_{vir} is the virial temperature of the core regions of the cluster (Peterson et al. 2001; Tamura et al. 2001). It is possible that gas below $T_{\text{vir}}/3 \sim 1 - 2$ keV is present but not detectable. For example, Fabian et al. (2001) discusses a model in which there are strong metallicity inhomogeneities and the high metallicity gas cools below 1–2 keV too rapidly for detection. No compelling model for the creation of such inhomogeneities exists, however. Additionally, a genuine lack of cool gas would help explain (and indeed may be *required* to explain) the deficiency of massive galaxies that is revealed while comparing the galaxy mass function and the dark matter halo mass function (Benson et al. 2003).

The cooling flow problem can clearly be solved if some phenomenon heats the ICM core enough to, on average, balance radiative cooling. A leading possibility is that jets from active galactic nuclei (AGN) at the center of galaxy clusters somehow provide this heating. It has been well established that AGN undergo complex interactions with the surrounding ICM, resulting in cavities (Fabian et al. 2000; McNamara et al. 2000; Blanton et al. 2001; Young et al. 2002; Nulsen et al. 2005b), ghost cavities (Fabian et al. 2000; McNamara et al. 2001; Heinz et al. 2002; Choi et al. 2004), ripples (Fabian et al. 2003, 2005), shells (Fabian et al. 2000), shocks (Jones et al. 2004; Nulsen et al. 2005a,b), and filaments (Nulsen et al. 2005b). It is feasible that one or several of these interactions result in the required heating.

In this paper, we present a new and moderately deep Chandra observation of the cooling core cluster Abell 4059 (A4059; $z = 0.049$). Previous X-ray studies have shown that A4059 has a double peaked surface brightness distribution, with a bright ridge of X-ray emission located to the southwest of the cluster center (Huang & Sarazin 1998; Heinz et al. 2002; Choi et al. 2004). This ridge seems to be in pressure balance with the ambient material. At the western boundary of this ridge there is a sharp gradient in temperature and density. It was suggested that this gradient could be explained by radiative cooling resulting from an interaction between the ICM and the radio-galaxy induced disturbance. While the metallicity profile of A4059 was not clear from these previous studies, there was weak evidence that it peaks at roughly solar values in the center regions and decreases outwards (Choi et al. 2004).

Additionally, previous studies have shown two X-ray

¹ Astronomy Department, University of Maryland, College Park, MD 20742

⁴ Think Energy Inc., 6930 Carroll Avenue, Takoma Park, MD 20912

³ Astronomy Department, University of Wisconsin, Madison, WI 53706

cavities in the center of A4059. The northwest cavity is clearly visible and distinct, while the southeast cavity is more difficult to discern (Huang & Sarazin 1998; Heinz et al. 2002). These previous studies found no evidence of shocks around the cavities. It was noted however that the axis connecting the centers of the two cavities does not pass through the position of the AGN itself, instead passing to the northeast of the galactic nucleus by $\sim 10''$. This prompted Heinz et al. (2002) to suggest that the radio-galaxy outburst erupted into an ICM that possessed a pre-existing bulk flow, and that the cavities have been pushed in the NE direction by that flow.

High-frequency radio studies (1.4 – 8.5 GHz) of this cluster indicate the presence of two radio lobes (Choi et al. 2004; Taylor et al. 1994) associated with the radio galaxy PKS2354–35. The northwest lobe only partially covers the northwest X-ray cavity, and the southeast lobe simply misses the southeast X-ray cavity. Both X-ray cavities are therefore ghost cavities, probably formed from a previous powerful burst of activity by the central FR I radio galaxy, PKS 2354-35 (Heinz et al. 2002; Choi et al. 2004). This has been recently confirmed by the detection of low frequency (330 MHz) radio emission coincident with these cavities (T. Clarke, private communication).

As we discuss in this paper, our new *Chandra* data change our view of this cluster. Section 2 describes the *Chandra* observations and basic data reduction. Section 3 discusses additional data reduction and presents X-ray images, temperature and metallicity maps, and the results of the deprojection analysis. The results are discussed and interpreted in § 4. In particular, we discuss how considerations of the metallicity asymmetry in A4059 leads us to a rather novel view of radio-mode feedback in this cluster. Finally, we present our conclusions in Section 5. Throughout this paper, we use J2000 coordinates and assume a standard WMAP cosmology (flat universe with $\Omega_\Lambda = 0.73$, $H_0 = 71 \text{ km s}^{-1} \text{ Mpc}^{-1}$; Spergel et al. 2003). Given the redshift of A4059/PKS2354–35 of $z = 0.04905$, this gives a luminosity distance of 215.1 Mpc and a scale of 0.95 kpc per arcsecond (Wright 2006)⁴.

2. OBSERVATIONS AND DATA REDUCTION

Chandra observed Abell 4059 on three separate occasions; 24-September-2000 (total exposure 24.6 ksec), 4-January-2001 (total exposure 20.1 ksec), and 26/27-January-2005 (total exposure 93.6 ksec). Results from the first two, shorter, observations have already been presented by Heinz et al. (2002) and Choi et al. (2004). All observations were performed with the Advanced CCD Imaging Spectrometer (ACIS) placing the core of the cluster close to the telescope aim-point on the central back-illuminated chip (i.e., chip S3). All data were reduced with CIAO version-3.4. The level-1 data were processed in order to apply the latest gain correction map as well as the latest version of the charge transfer inefficiency (CTI) correction. The processed level-1 data were then filtered with a standard grade selection (including ASCA grades 0,2,3,4,6) resulting in new level-2 events lists. Periods of high background were searched for by examining the chip-S1 lightcurve. The September-2000

data were found to be affected by a large background flare; elimination of the affected data reduced the good exposure time to 16 ksec. The 2001 and 2005 data were not affected by significant background flares, allowing the full 24.6 ksec and 93.6 ksec, respectively, to be utilized.

The three datasets (totaling 134.2 ksec of usable data) were merged using the `merge_all` script in CIAO. A $4.2' \times 4.2'$ (238 kpc \times 238 kpc) region enclosing the cluster core was extracted to create an exposure-corrected image. It would, however, be inappropriate to use the merged dataset for spectral studies. The spectral response of the ACIS depends on the chip coordinates, which map to different physical coordinates for the three observations. Additionally, the spectral response has degraded with time due to a slow increase in charge transfer inefficiency (CTI) and the build-up of a contaminant on the ACIS filter. For these reasons, spectral studies are only performed on the 2005 data. Given that the 2005 observation corresponds to 70% of our total good data for this object, this restriction does not significantly impact the signal-to-noise of our spectral study.

3. ANALYSIS AND RESULTS

3.1. X-ray Images

Figure 1 shows the exposure-corrected full-band (0.3–10 keV) unsmoothed image of A4059. The double peak (corresponding to the cluster core and the SW ridge) is prominent, and the northwest cavity is clearly visible. A spur of bright emission is seen to the southwest of the core. The improved signal-to-noise allow previously unknown aspects of the morphology to be discerned. The core of the cluster and the SW ridge are clearly connected in the north by a high-contrast curved rim. This rim appears to continue through the brightest part of the SW ridge and define the southern parts of the ridge. Although much less distinct, there may be a similar structure which is the approximate reflection of this rim in the line joining the cluster core and the brightest part of the SW ridge. At a much lower contrast, one can trace a thin plume extending from the core directly northwards for 60 kpc (1 arcmin), and another plume extending northwest from the SW ridge.

From the merged data, we produced adaptively smoothed, exposure-corrected, full band (0.3-10 keV) images using the CIAO tool `csmooth`. Significance levels in the range $3 - 5\sigma$ were used to set the smoothing scales. The adaptively-smoothed image shown in Fig. 2 supports earlier morphological studies of Abell 4059. While the outer portion of the cluster is fairly relaxed, the inner 60 kpc is rather disturbed showing the cavities and southwest ridge that have been well studied in previous works. Our deeper image reveals new structure, however. The adaptively smoothed image hints at part of a shell bounding the disturbed region of the cluster, especially to the southeast of the cluster.

To investigate this apparent shell in more detail, we created an unsharp-mask image following the approach of Fabian et al. (2003). In detail, images with two different Gaussian smoothings were created from the merged data, one image with a Gaussian smoothing scale of 25 pixels (12.5'') and the other with a Gaussian smoothing scale of 3 pixels (1.5''). The unsharp-mask image was created by subtracting the heavily smoothed image from the lightly

⁴ <http://www.astro.ucla.edu/~wright/CosmoCalc.html>

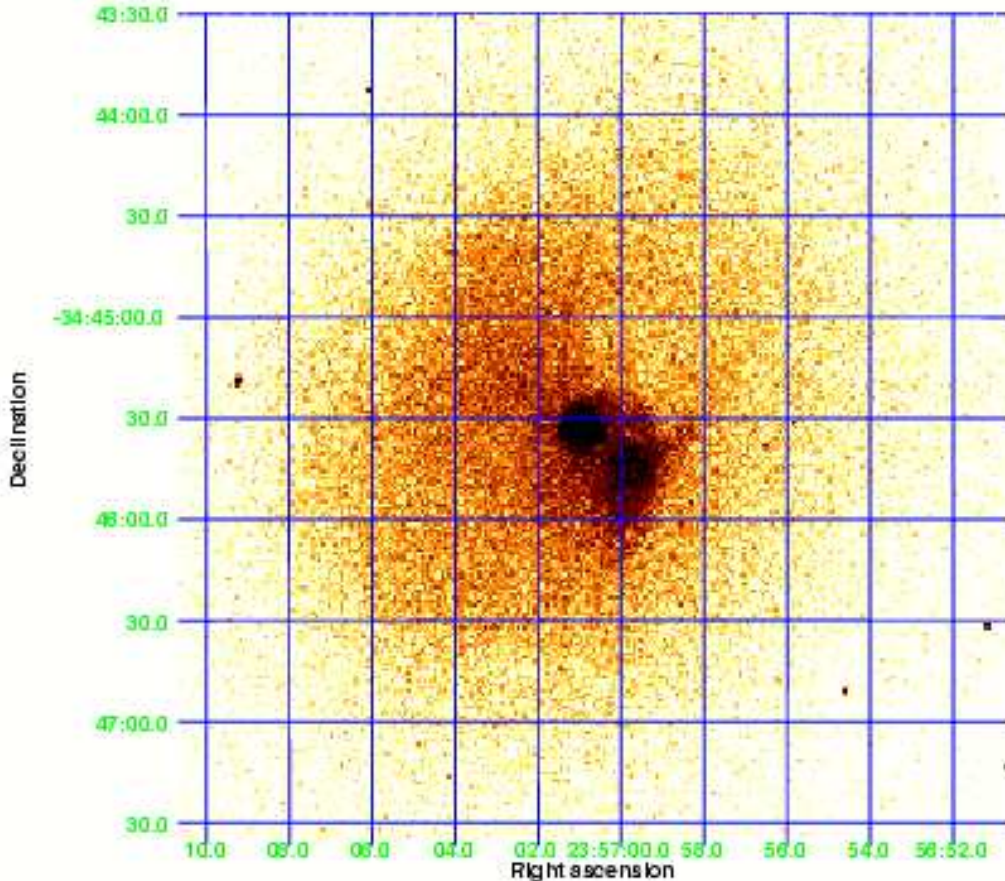


FIG. 1.— Exposure-corrected full-band (0.3–10 keV) image of A4059.

smoothed image, a process which allows one to search for subtle discontinuities in either the surface brightness or the gradient of the surface brightness. The result is shown in Fig. 3, and reveals a subtle “edge” which has an approximate semi-circular form in the eastern and northern quadrants. The projected radius of this feature is 70–80 kpc. There are hints that, once this edge crosses the jet axis, this feature may sweep inwards and connect onto each end of the SW ridge.

Another view of this structure is obtained by constructing radial surface brightness profiles. Figure 4 shows the surface brightness profile for a sector of the cluster between position angles 225° and 270°. This sector cuts the edge noted in the unsharp-mask image at a distance of 80 kpc from the cluster center and, indeed, a small discontinuity in gradient of the surface brightness can be seen at $r = 80$ kpc. Unfortunately, further studies of this feature (e.g., searching for temperature jumps associated with the surface brightness jump) are beyond what is possible with the current dataset. Rigorously characterizing the nature of this feature must await significantly deeper X-ray data. However, by analogy with findings in other systems (e.g., Virgo; Forman et al. 2007), it

seems likely that this feature is a weak shock or compression wave driven into the ICM by the radio galaxy activity. In § 4, we discuss the implications of this hypothesis for the age of the AGN. As noted in Markevitch et al. (2000), a curved shock/compression front viewed in projection does *not* produce a true discontinuity in the surface brightness but, instead, is revealed through a discontinuity in the gradient of the surface brightness of the kind suggested by Fig. 4.

3.2. Imaging Spectroscopy Using Adaptive Binning

By examining the spectrum of the X-ray emission across the image, the spatial distribution of temperature, metallicity, density, pressure, and entropy can be probed. This kind of physical information is crucial if we are to disentangle this complex source. In particular, understanding the spatial distribution of metals in this cluster is a major motivation for these new data.

Spectral analysis was performed on data that had been adaptively binned using the Weighted Voronoi Tessellation (WVT) binning algorithm of Diehl & Statler

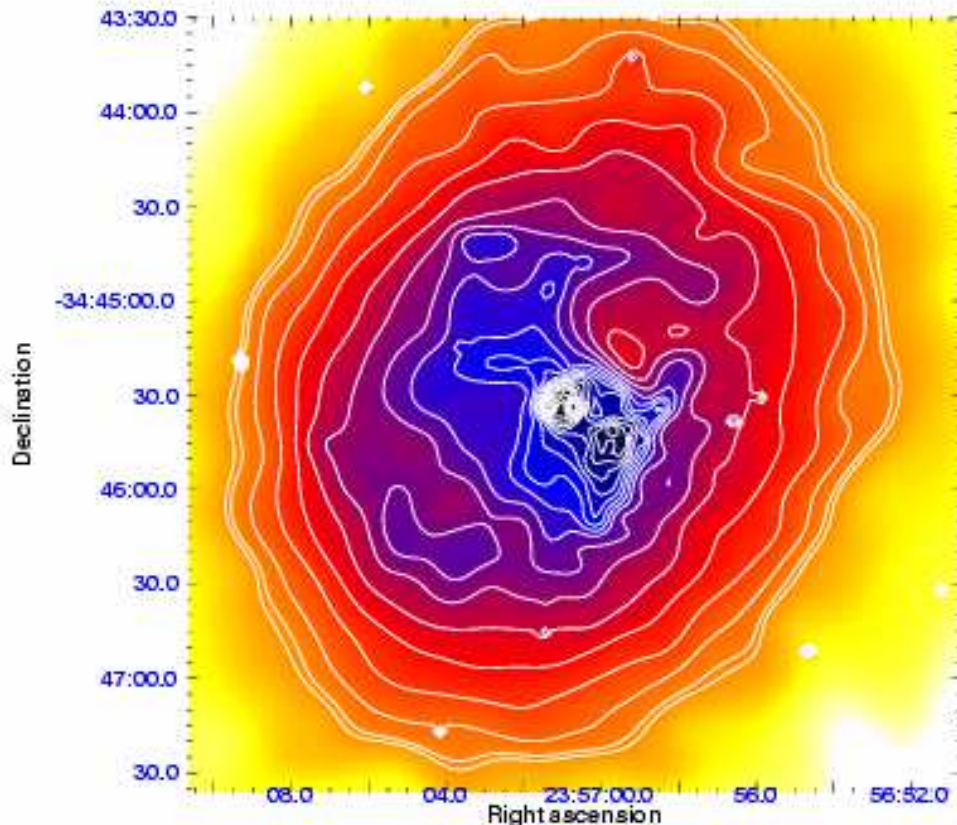


FIG. 2.— Adaptively-smoothed, exposure corrected image of the core regions of A4059. Logarithmically-spaced contours of this same map are also over-laid.

(2006)⁵. This algorithm produces polygonal bins with a constant signal to noise ratio (SNR), where the number of photons in each bin is the square of the prescribed SNR. Once the optimal polygon-tiling of the image plane has been determined, the CIAO tool `specextract` was used to extract spectra, energy response matrices and effective area curves for each tile. A single background spectrum was obtained from the source free region at the north-east corner of the S3-chip. After experimentation, we determined that a SNR of 30 allows us to construct adequate maps of plasma temperature and emission measure (and hence density, pressure and entropy). Metallicity maps requires higher quality spectra and could only be constructed once the SNR was increased to 40.

The spectrum from each bin was modeled using a single temperature thermal plasma model `mekal` (Mewe et al. 1985, 1986; Kaastra 1992; Liedahl et al. 1995) modified by the effects of Galactic photoelectric absorption with column density $N_{\text{H}} = 1.45 \times 10^{20} \text{ cm}^{-2}$. The abundance of metals within the plasma was a free parameter of the spectral models. However, the relative abundance of all elements heavier than helium was fixed at their cosmic ratios (Anders & Grevesse 1989); no statistical improve-

ment in the fit is obtained by relaxing this assumption. Spectral fitting was performing using XSPEC version 11.3.2. Although we formally fit the 0.5–10 keV data, the spectra of most tiles become background dominated about 7 keV. The absorption column was held fixed for the spectral fitting presented here, although we have confirmed that our results are robust to allowing N_{H} to be a free parameter.

The temperature map (made from the SNR = 30 tessellation) is shown in Fig. 5 (top panels). The most obvious feature in this map is the region of cool (< 2.5 keV) gas that extends from the core through the SW ridge. Examination of this temperature map shows that cool gas has a close spatial correspondence with the highest surface brightness regions of the SW ridge. In particular, the boundary of the region containing the cool gas closely follows the high-contrast curved rim of emission that connects the core with the SW ridge (see discussion in § 3.1), and continues to track this curved rim through the SW ridge and into the southern extremity of the SW ridge. Interestingly, the spur that projects from the SW ridge in the north-westerly direction is appreciably hotter than the rest of the SW ridge (3.5–4.0 keV as opposed to 2.0–2.5 keV).

For the first time, these data allow us to examine the 2-

⁵ <http://www.phy.ohiou.edu/~diehl/WVT>

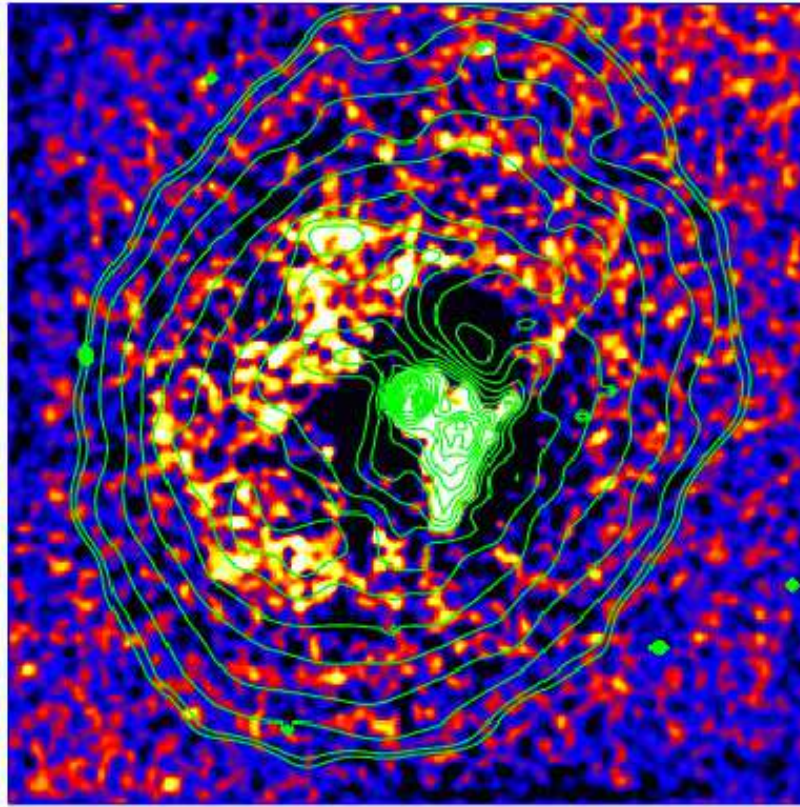


FIG. 3.— Unsharp mask image of A4059, created by subtracting a full band map smoothed with a $\sigma = 12.5''$ Gaussian from a map smoothed with a $\sigma = 1.5''$ Gaussian. Overlaid are contours of the adaptively-smoothed map.

dimensional metallicity distribution for this cluster. The metallicity map derived from single temperature thermal plasma fits (using the SNR = 40 map) is shown in Fig. 5 (middle panels). The most significant feature in this map is the dramatic enhancement in metallicity (upto twice the average cosmic abundance) along the SW ridge. Metal enriched gas appears to be present along the en-

tire length of the SW ridge, including the north-westerly spur which was noted above to be at a significantly higher temperature than the rest of the SW ridge. It is particularly striking in this map that the metallicity of the SW ridge appears to be appreciably higher than that of the central core itself.

The picture concerning the metallicity distribution in the centralmost regions changes somewhat, however, when we go beyond a single temperature thermal plasma model for the spectrum of each bin. In particular, we have fitted spectra from the tiles of the SNR = 40 tessellation with a two-component thermal plasma model; the temperature and emission measure of each plasma component is a free parameter of the fit, but the two components are assumed to share a common metallicity. Comparing the χ^2 goodness of fit parameter for the single-component and two-component plasma models, we find that the two-component model is not a statistically better description of the data than the single-component model (employing the F-test for two additional model parameters) for the spectrum from *most* of the tiles, *including those that make up the SW ridge*. Furthermore, for this vast majority of tiles, the best-fitting value of the metallicity parameter is similar between the single-temperature and two-temperature fits. This last result is unsurprising since, in most cases, the normalization (emission measure) of one of the plasma components in these two-component fits vanishes, leaving essentially a single temperature fit. The spectra from the tiles in the centralmost bins of the cluster are, however, described significantly better (at the 90% or more level) by the

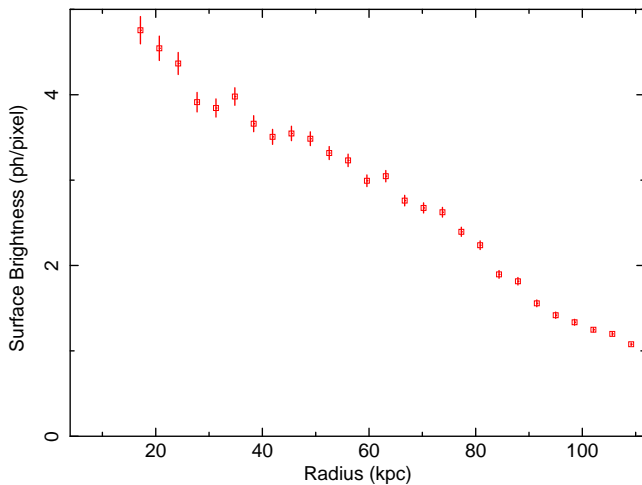


FIG. 4.— Surface brightness profile for a sector of the cluster between position angles 225° and 270° (i.e., the ESE sector).

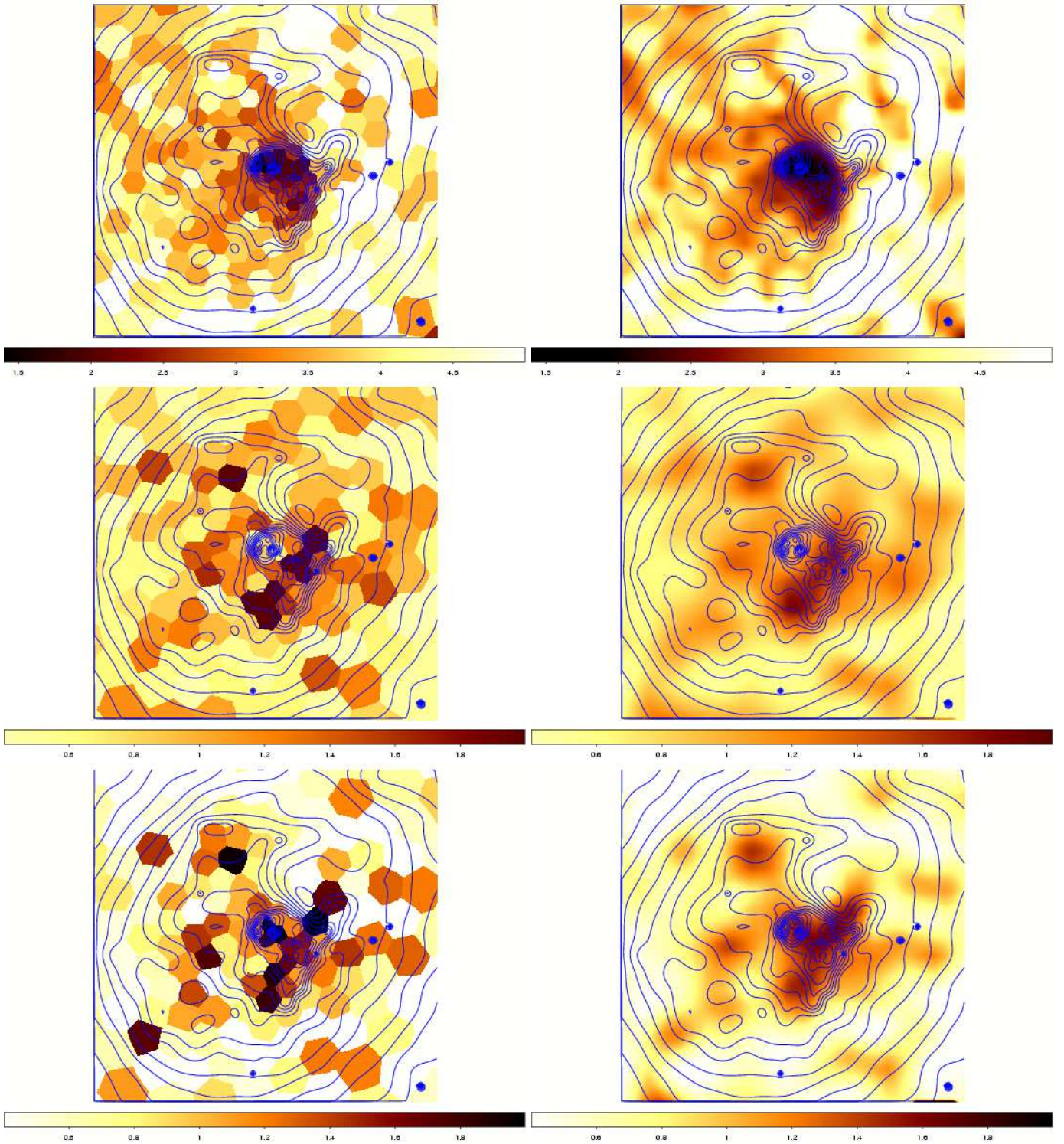


FIG. 5.— *Top left panel* : Temperature map of the core regions of A4059 based on the SNR = 30 Voronoi Tessellation. Color-bar units are keV. *Top right panel* : Smoothed temperature map, using a $20''$ box-car smoothing kernel. *Middle left panel* : Metallicity map (based on single temperature fits) of the core regions of A4059 based on the SNR = 40 Voronoi Tessellation. Color-bar units are cosmic abundances (as defined by Anders & Grevesse 1989). *Middle right panel* : Smoothed (single temperature) metallicity map, using a $40''$ box-car smoothing kernel. *Bottom left panel* : Metallicity map (based on two-temperature fits) of the core regions of A4059 based on the SNR = 40 Voronoi Tessellation. Color-bar units are cosmic abundances (as defined by Anders & Grevesse 1989). *Bottom right panel* : Smoothed (two-temperature) metallicity map, using a $40''$ box-car smoothing kernel.

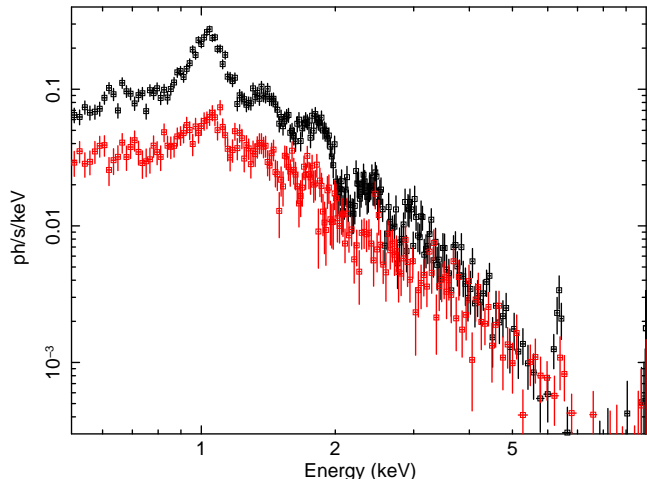


FIG. 6.— The 0.5–10 keV spectra of an elliptical region encompassing the SW ridge (upper spectrum; black points) and an off-ridge region of the same size located $12''$ to the south-west of the SW ridge (lower spectrum; red points). Note that the iron-L complex at 1 keV and the iron-K line at ~ 6 keV are appreciable stronger in the ridge spectrum.

two-component plasma model. The need for these multi-temperature models may reflect the morphological complexity of the ICM center or the combined contributions from both the core of the ICM and the ISM of the cD galaxy itself.

It is important to assess the effect of the multi-component model on the inferred temperature and metallicity distributions. We find that the one-component temperature maps shown in Fig. 5 (top panels) remain an accurate approximation to the *emission-measure weighted* temperature map derived from the two-component fit. On the other hand, the metallicity of the core inferred from the two-component fits is appreciably higher than that inferred from the single-temperature fits ($Z = 1.2 - 2Z_{\odot}$ compared with $Z = 0.6 - 1.0Z_{\odot}$). The metallicity map derived from the two-component plasma fits Fig. 5 (bottom panels) still show a notable enhancement of metallicity along the SW ridge, but the metallicity enhancement now also extends into the regions immediately surrounding the cD galaxy.

To demonstrate the robustness of the conclusion regarding the high abundance of the SW ridge, we have extracted the 0.5–10 keV spectrum from a single elliptical region ($25'' \times 10''$) that encompasses the whole SW ridge and compared it with the spectrum from the same sized region located $12''$ to the south-west (i.e., beyond the SW ridge). One and two temperature thermal plasma fits to the SW-ridge spectrum implies a metallicity of $Z = 1.70 \pm 0.18Z_{\odot}$ and $Z = 1.84^{+0.29}_{-0.27}Z_{\odot}$, respectively. On the other hand, one and two temperature fits to the non-ridge spectrum yields $Z = 0.87 \pm 0.24Z_{\odot}$ and $Z = 0.83^{+0.34}_{-0.26}Z_{\odot}$, respectively. Indeed, this metallicity difference is visually apparent in the spectra; examination of the spectra (Fig. 6) reveals an iron-L line complex at ~ 1 keV and iron-K line at ~ 6 keV which are clearly stronger in the ridge spectrum than the off-ridge spectrum.

With some assumptions about the line-of-sight geometry, the emission measure can be used to compute the

characteristic density of the plasma contributing to the observed radiation from a given spatial bin. Operationally, the electron number density n_e is obtained from the normalization of the `mekal` component (N) in the one-temperature fits by

$$n_e = D_A(1+z)\sqrt{4 \times 10^{14}\pi NV^{-1}}, \quad (1)$$

where $D_A = 195$ Mpc is the angular size distance to A4059, $z = 0.049$ is the redshift, and V is the effective volume of the emitting plasma in that bin. The volume V was estimated by multiplying the area of the Voronoi tile by the distance to the cluster center, as defined by the location of peak brightness (which coincides with PKS 2354–35 itself). Given the density and spectrally determined temperature, the pressure is obtained from the ideal gas equation:

$$P = nkT. \quad (2)$$

where n is the total particle number density of the plasma, assumed to be given by $n = 1.93n_e$ (appropriate for 75% H and 25% He). The entropy index was calculated using

$$s = \frac{k_B T}{n_e^{\gamma-1}}. \quad (3)$$

where we assume a standard adiabatic index of $\gamma = 5/3$. Finally, we compute the radiative cooling timescale

$$\tau_{\text{cool}} \equiv \frac{3nkT}{2n_e n_H \Lambda(T)} \quad (4)$$

where n_H is the hydrogen number density, and $\Lambda(T)$ is the cooling function modeled using the fitting formula of Sutherland & Dopita (1993).

These maps of density, pressure, entropy index and cooling time are shown in Fig. 7. They show the expected trends; both density and pressure decrease with radius, while entropy and cooling time increases. It is particularly interesting to relate these physical quantities to the SW ridge. Given the improvement in the spatial resolution of our maps over those of Choi et al. (2004), we can spatially resolve variations of these physical quantities over this ridge. Confirming and strengthening the result of Choi et al. (2004), the pressure map is reasonably symmetric and does not show any discontinuity coincident with the SW ridge. Instead, the SW ridge corresponds to a region of denser, colder gas that maintains a sharp interface (with a thickness of < 5 kpc) with the surrounding hotter gas. The gas within the ridge has a cooling time of 500–700 Myr, compared with cooling times in excess of 1.5 Gyr in the ICM interfaces.

3.3. Deprojection Analysis

The 2-d spectral imaging analysis described above does not properly take into account the full 3-d nature of the cluster. Each bin will inevitably include contributions from gas that has a range of distances from the cluster center. Hence, any radial gradients of temperature, density and metallicity will mean that each bin could therefore include gases with different properties.

To assess the effect of this, we performed a standard deprojection analysis using the `project` command within XSPEC. The observed cluster emission was divided into 18 concentric, equal width annuli centered on the core

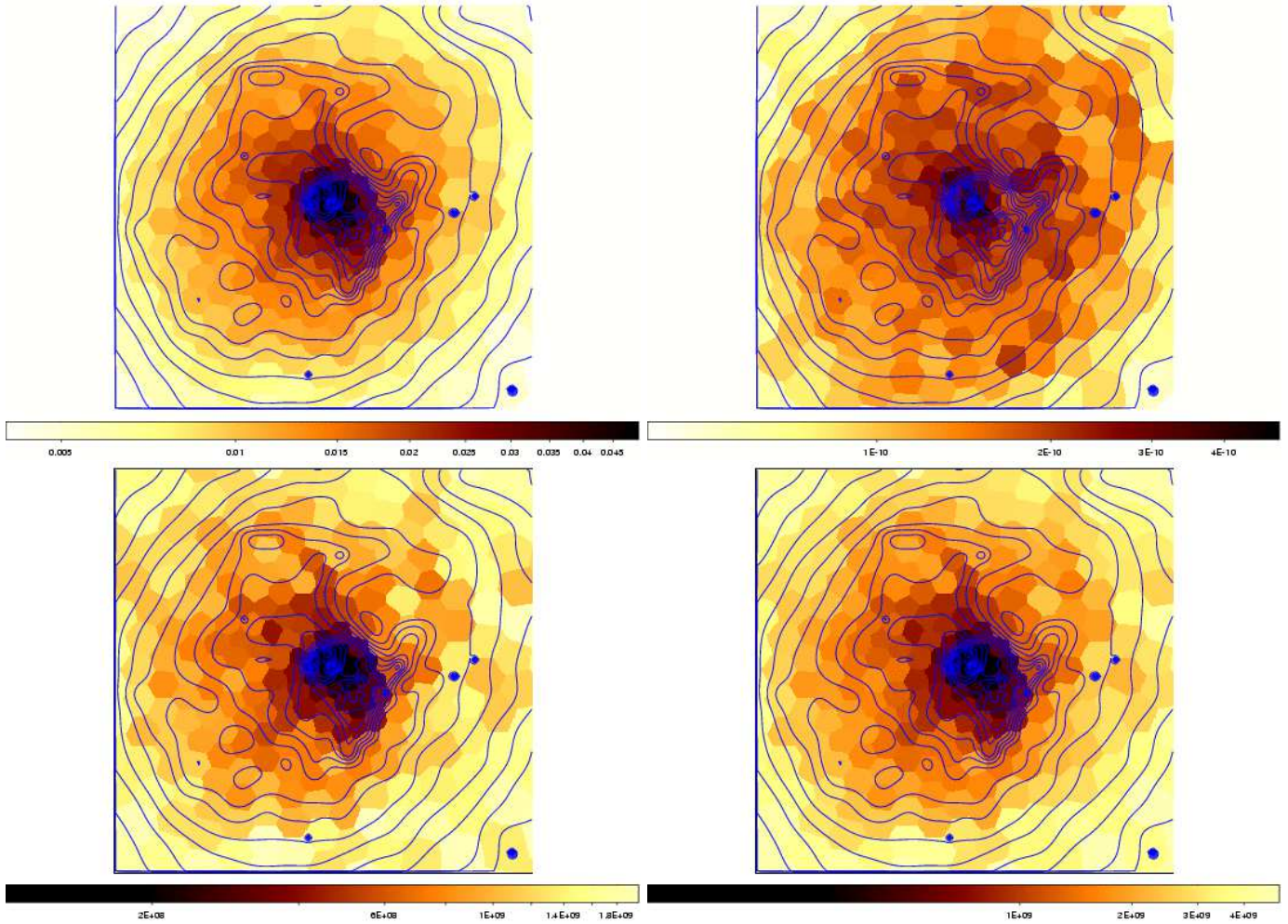


FIG. 7.— Maps of density (top-left), pressure (top-right), entropy index (bottom-left) and cooling time (bottom right). Color bar units are cm^{-2} (density), erg s^{-1} (pressure), K cm^{-2} (entropy index), and years (cooling time). Contours of the adaptively smoothed full-band surface brightness are overlaid.

of the cluster PKS2354-35. Assuming the cluster to be spherically symmetric (an assumption that clearly breaks down within the central region), we can “peel” spherical shells from the cluster; the spectrum from a particular shell has the contributions from more distant shells subtracted, thereby allowing one to model the spectrum of the gas only in that shell. We fitted each shell with a single temperature thermal plasma model (`mekal`) with absorption fixed at the Galactic value. The density of the gas in each shell was calculated from the emission measure (which is directly proportional to the best-fitting normalization of the `mekal` model) by assuming that the plasma uniformly filled the shell. The pressure and entropy index follows straightforwardly once the temperature and density are known.

The results of this deprojection are shown in Fig. 8. As in Choi et al. (2004), the temperature increases with radius, while the density and pressure decrease. The decrease is quite rapid along the inner radii. Between 10 and 40 kpc, a slight dip in the pressure is visible, probably due to the presence of the cavities. The deprojected metallicity results reflect the behavior seen in the spectral analysis of the 2-d (projected) data. The one-component

plasma fit implies a metallicity that is low at the center, increases to a maximum at ~ 25 kpc (corresponding to the metal rich SW ridge entering the annuli under consideration) and then decreases again at large radii. As in the case of the projected spectral analysis, this central “hole” in the metallicity is removed when a second plasma component (with a different temperature but in pressure equilibrium and with a common metallicity) is introduced (Fig. 9).

4. DISCUSSION AND CONCLUSIONS

The jet axis of the central radio galaxy PKS 2354-35 is oriented on a SE to NW line, and this system has approximate reflection symmetry about a line passing through the AGN perpendicular to the jet axis; i.e., the jet and counter-jet sides look rather similar. However, this system shows striking asymmetries in the direction lateral to the jet axis. These new data uncover several new aspects of this asymmetry that were beyond the reach of the previous analyzes of Heinz et al. (2002) and Choi et al. (2004).

Firstly, both the unsharp mask image (Fig. 3) and the radial surface brightness profile (Fig. 4) reveals a subtle discontinuity in the gradient of the surface bright-

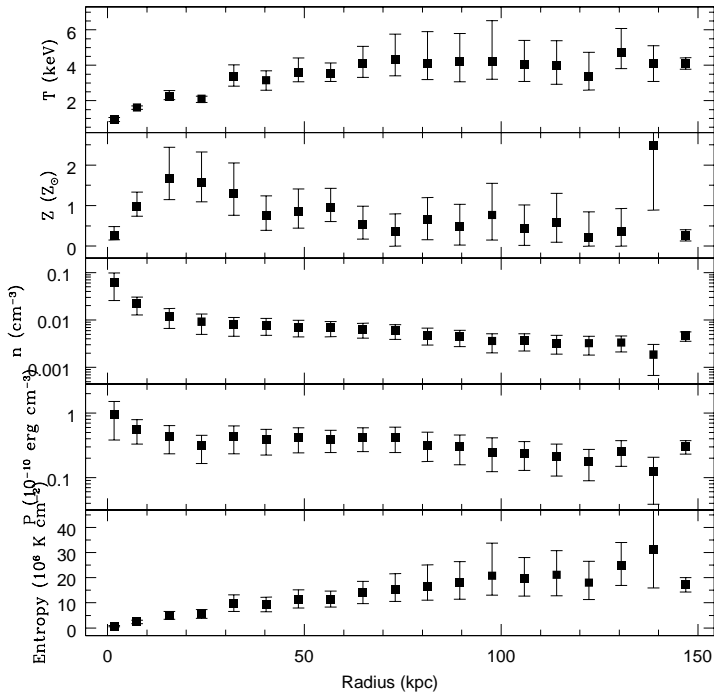


FIG. 8.— Single temperature deprojection analysis for A4059.

ness that is approximately semi-circular in form (with 60–80 kpc radius) and centered on the radio galaxy. The previous *Chandra* observations reported by (Heinz et al. 2002; Choi et al. 2004) had insufficient signal to detect

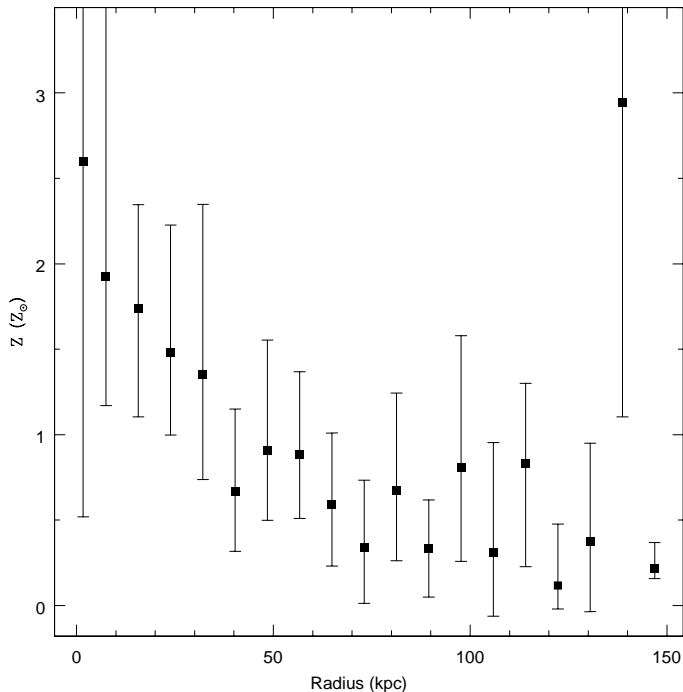


FIG. 9.— Metallicity distribution obtained from the two-component thermal plasma model fitted to the deprojected data for A4059.

this feature. Although it cannot be rigorously proven from these data, it seems reasonable to interpret this as a weak shock driven into the previously undisturbed ICM by the onset of radio galaxy activity; such shocks are seen in all hydrodynamic simulations of jet/ICM interactions (e.g., Reynolds, Heinz & Begelman 2002; Vernaleo & Reynolds 2006, 2007 and references therein), and have been found by *Chandra* in Hydra A (Nulsen et al. 2005) and Virgo (Forman et al. 2007). Assuming that the velocity of this front through the ICM is greater than the local sound speed c_s and that the ICM is at rest with respect to the cD galaxy, we can estimate an upper limit on the time since the initial radio galaxy activity launched the shock. If L is the current distance between this shock front and the AGN, and t is the time since the onset of radio-galaxy activity launched the shock, we have

$$L > \int_0^t c_s dt, . \quad (5)$$

Using the deprojected temperature profile to determine $c_s(r)$, we determine that $t < 90$ Myr. This compares well with estimates for the source age based on the buoyant rise time of the X-ray cavities (Heinz et al. 2002). We note, however, that we only see this feature on the NE side of the jet line; there is no similar feature on the SW side. This may be due to the simple fact that the ICM emission on the SW side of the cluster is fainter than the NE side and, hence, the putative shock is below our detectability limit.

Secondly, the temperature map shows that the ICM temperature distribution is strongly asymmetric. A convex cold front (i.e., boundary across which there is a discontinuity in temperature but continuity in pressure) seems to extend from the central core through highest surface brightness portions of the SW ridge. This cooler and denser material has a comparatively short radiative cooling time, only 500–700 Myr. We note that this is rather longer than the central/ridge cooling times inferred by Choi et al. (2004); we consider our cooling time map to be more robust given that we have the signal to noise to produce a map in which the gross morphological structures are resolved [in contrast to Choi et al. (2004) who could only examine cooling times within bins that combined core and SW ridge emission]. One important qualitative difference is that our inferred cooling times are almost an order of magnitude longer than the plausible age of the radio source, eliminating the possibility discussed in Choi et al. (2004) that the SW ridge is cool due to compression-enhanced radiative cooling.

Thirdly, our new data allow us to map the 2-dimensional distribution of metals and reveal that it, too, is strongly asymmetric. High metallicity gas appears to extend along the length of the SW ridge, including into the NW spur of the SW ridge that lies beyond the cold front and may form the wall for the northern cavity. The result that the SW ridge possesses enhanced metallicity is robust in both one-component and two-component thermal plasma fits. We do find, however, that the apparent drop in metallicity within the central core that is inferred from one-component fits is removed when one considers two-component plasma fits.

Assuming that the jet production process itself is axially symmetric, all of the evidence points to an ini-

tial (pre-interaction) ICM atmosphere that was strongly asymmetric. The asymmetries in this system have previously been interpreted in terms of a bulk flow within the ICM (flowing in the plane of the sky from the SW to the NE) prior to the onset of powerful radio galaxy activity. However, it is very hard to understand the metallicity asymmetry in terms of such a bulk flow. Instead, it seems likely that an anomalously dense, cool, metal-rich region of gas was situated to the SW of the center of the cD galaxy at the time that the AGN initiated its jet activity. This anomalous region would have been weakly shocked and possibly pushed higher into the ICM atmosphere by the laterally expanding radio galaxy cocoon, thereby forming the SW ridge. If this scenario is correct, it seems that some fraction of this metal rich gas has been entrained into the walls of the X-ray cavities, especially in the NW direction.

At this point, it is useful to estimate the mass of gas within the SW ridge and the gravitational potential energy of this structure. The brightest region of the (projected) SW ridge emission can be encompassed by an ellipse with major and minor axes of 15 arcsec and 8 arcsec respectively. Assuming that this is a oblate spheroid in projection, we estimate the emitting volume to be $V = 2 \times 10^{68} \text{ cm}^3$. A single-component thermal plasma fit provides an adequate description of the data and implies a total emission measure of

$$EM \equiv \int_V n_e^2 dV \approx 1 \times 10^{65} \text{ cm}^{-3}. \quad (6)$$

Assuming that twice cosmic abundance plasma uniformly fills this region, we conclude that the total mass of ICM within this ridge is $M \sim 5 \times 10^9 M_\odot$. We can also estimate the energy required to lift this matter from a location close to the center of the cD galaxy to its current position in the gravitational potential. Assuming that the undisturbed ICM is approximately isothermal with sound speed c_s and is in a hydrostatic configuration with density profile $\rho(\mathbf{r})$, integration of the equation of hydrostatic equilibrium gives the gravitational potential,

$$\Phi = \frac{c_s^2}{\gamma} \ln \left(\frac{\rho}{\rho_0} \right), \quad (7)$$

where $\gamma = 5/3$ is the ratio of specific heat capacities and ρ_0 is some fiducial density that plays the role of the (uninteresting) constant of integration. The change in gravitational potential energy when mass M is lifted within the atmosphere is given by

$$\Delta E = M \Delta \Phi = \frac{M c_s^2}{\gamma} \ln \left(\frac{\rho_1}{\rho_2} \right), \quad (8)$$

where ρ_1 and ρ_2 are the densities of the undisturbed ICM atmosphere at the start point and end point, respectively, of the lifting process. Using values of $c_s \approx 700 \text{ km s}^{-1}$ (corresponding to the $kT \approx 2 \text{ keV}$ plasma that characterizes the central regions of the ICM), and $\rho_1/\rho_2 \sim 5$ (from the deprojection results), we obtain $\Delta E \sim 5 \times 10^{58} \text{ erg}$. To place this energy into context, Heinz et al. (2002) estimated that the energy required to inflate the observed X-ray cavities exceeded $8 \times 10^{59} \text{ erg}$, almost 20 times greater than the energy required to lift the cool gas in the SW ridge.

While it seems clear that the ICM atmosphere was asymmetric prior to the (most recent) onset of radio galaxy activity, the cause of that asymmetry is unclear. One possibility is that the asymmetry was caused by the merger/assimilation of A4059 with a small galaxy cluster or group. The SW ridge could then be identified with the remains of the ICM core of the smaller subcluster (albeit with a morphology that has been subsequently shaped by interaction with the jet-blown cocoon of PKS 2354–35). Indeed, Heinz et al. (2003) have shown that some fraction of ICM cold fronts are likely to be associated with subcluster merger events, and that the hydrodynamics of such an interaction can cause high metallicity gas to be dredged up from the center of the merging core and carried up to the cold front. This would qualitatively provide a natural explanation for the high metallicity of the SW ridge. The gross X-ray morphology of A4059 is also reminiscent of the “X-ray comet tail” found in the Abell 2670 cluster (Fujita, Sarazin & Sivakoff 2006). The mass of the gas in the “comet tail” is similar to the SW ridge in A4059, and it also appears cooler than the ambient ICM. In the case of A2670 the association of the “comet tail” with a large elliptical galaxy, and the high peculiar motion of the cD galaxy, makes it very plausible that we are witnessing the merger of a small cluster or group with A2670 and that the comet-tail is the distorted/stripped remnants of the subcluster’s ICM core.

The subcluster merger scenario faces two potential problems. Firstly, unlike the case of A2670, there is no obvious association of the SW ridge with any galaxy. Since the galaxies associated with the merging subcluster may have left behind their ICM core (such as is seen in the Bullet Cluster 1E 0657–56; Markevitch et al. 2002), this fact by itself does not rule out the merging subcluster hypothesis; it does predict, however, that a detailed mapping of the galaxy dynamics in this cluster should reveal a kinematically distinct subcluster. Secondly, the metallicity of the SW ridge is $1.5 - 2 Z_\odot$, an extreme value if this is to be identified with the ICM core of a merging subcluster (Baumgartner et al. 2005; Snowden et al. 2007). Hence, while the merging subcluster hypothesis cannot yet be ruled out, we are led to explore other scenarios.

The very high metallicity of the SW ridge, in particular, pushes us to explore scenarios in which the gas originates directly from the metal enriched ISM of an actively star-forming galaxy. In order to deposit $5 \times 10^9 M_\odot$ of metal rich gas into a localized region of the cluster, the donor galaxy must have been massive (comparable to or greater than an L^* galaxy) and the stripping mechanism must have been efficient and rapid. One possibility is that a large gas-rich late-type galaxy plunged through the core of A4059 for the first time and underwent an intense compressionally-driven starburst (Reverte et al. 2007). The combination of the starburst-driven superwind and ram-pressure stripping by the ICM could have allowed the galaxy to dump the required amount of metal-rich gas on a timescale short compared with the time taken to traverse the cluster core. Essentially, the star-bursting galaxy would leave a “debris” trail behind it comprising of metal rich, relatively cool, possibly multiphase gas. We hypothesize that this debris trail is the high-metallicity inhomogeneity which, once impacted by the radio-galaxy activity, produces the SW ridge feature in

A4059.

If the projected (i.e., plane of the sky) velocity of the galaxy during its passage through the cluster core is $v = 1000v_3 \text{ km s}^{-1}$, the metal rich ISM would have to be stripped from the galaxy at a rate exceeding $200v_3 \text{ M}_\odot \text{ yr}^{-1}$ in order to produce a distinct region consisting of $5 \times 10^9 \text{ M}_\odot$ of metal-rich gas that is only $\sim 25 \text{ kpc}$ in projected extent. Once stripped away from the galaxy, this denser gas will follow a decaying orbit within the (dark matter dominated) gravitational potential due to the action of gas drag. Concurrently, hydrodynamic instabilities will tend to mix this stripped gas with the ambient ICM. Detailed theoretical modeling beyond the scope of this paper is required in order to estimate the time over which the starburst-delivered gas will remain a distinct inhomogeneity within the ICM core. For now, we estimate an upper limit on the time since this starburst/stripping event occurred by equating it with the orbital time of the gas within the potential, $\tau \sim 2\pi\sqrt{r/g}$, where $g \equiv -\nabla\Phi$ is the acceleration due to gravity in the cluster potential. This timescale is within a factor of order unity the same as the time taken for the cooler gas to fall radially into the center of the potential. Assuming that the underlying ambient ICM density field is approximately spherically symmetric $\rho = \rho(r)$, we have

$$g = -\frac{c_s^2}{\gamma r} \frac{r d\rho}{\rho dr}, \quad (9)$$

and we see that

$$\tau \sim 2\pi\sqrt{\frac{r^2\gamma}{c_s^2(-r d\rho/\rho dr)}}. \quad (10)$$

Putting $r = 25 \text{ kpc}$, and noting that $-r d\rho/\rho dr \sim 1 - 2$, we estimate that the starburst/stripping event occurred at most $\tau \sim 200 - 300 \text{ Myr}$ ago.

An obvious and important prediction of this starburst-stripping hypothesis is that the responsible galaxy should still be in the vicinity and should still display post-starburst signatures. Using the above estimate of the upper limit on the time since the starburst/stripping event, the post-starburst galaxy should still be within a projected distance of $300v_3 \text{ kpc}$ of the cluster core. This corresponds to an angular distance of $285v_3 \text{ arcsec}$. Of course, deceleration of the galaxy as it climbs out of the dark matter potential would reduce this distance.

A systematic study of the optical spectrum of the member galaxies of A4059 is required in order to find the post-starburst galaxy predicted by this hypothesis. One interesting candidate, however, is the bright spiral galaxy ESO 349-G009 situated $280''$ directly to the north of the cD galaxy ESO 349-G010 (see Fig. 10). The radial velocity difference between ESO 349-G009 and ESO 349-G010/PKS2354-35 is almost $\Delta v = 2100 \text{ km s}^{-1}$ ($v = 12612 \text{ km s}^{-1}$ for ESO 349-G009 compared with $v = 14705 \text{ km s}^{-1}$ for ESO 349-G010/PKS2354-35; de Vaucouleurs et al., 1991) implying that this late-type galaxy is either simply a foreground object or a high-velocity galaxy close to the A4059 cluster. From the absolute 2MASS K-band magnitude of $M_K = -25.82$, we can assume a K-band stellar-mass to light ratio of 0.7 (Bell et al. 2003) and a solar K-band absolute magnitude of 3.27 (Holmberg et al. 2006) in order to derive an estimate

for the stellar mass of this galaxy, $M_* \approx 3 \times 10^{11} \text{ M}_\odot$. Thus, we see that the SW ridge in the ICM core could have been formed via the ejection of gas totaling a few percent of the stellar mass.

What makes ESO 349-G009 a particularly interesting candidate is the presence of X-ray and near ultraviolet (NUV) evidence for on-going vigorous star formation. Sun et al. (2007) present an analysis of the X-ray emission from ESO 349-G009 using the same *Chandra* data as reported upon here. They find a luminous (spatially resolved) X-ray corona associated with the galactic bulge in addition to three point sources associated with the spiral arms (Fig. 11). They also note that, despite the absence of an AGN (i.e., an unresolved source at the location of the galactic nucleus) in this galaxy, the X-ray emission has a hard component with $L_{2-10 \text{ keV}} = 0.8 - 2.7 \times 10^{41} \text{ erg s}^{-1}$. Associating the hard X-rays with High Mass X-ray Binaries, they use the correlation of Grimm, Gilfanov & Sunyaev (2003) to estimate a star formation rate of $> 12 \text{ M}_\odot \text{ yr}^{-1}$. This conclusion is supported by the fact that ESO 349-G009 is luminous in the NUV band (see Fig. 26 of Sun et al. 2007). Within the context of our starburst-stripping hypothesis, one can postulate a scenario in which ESO 349-G009 executed a high velocity plunge through the core of A4059 and suffered an intense ICM-pressure induced starburst which is still in the process of dying away. High-quality optical spectroscopy of ESO 349-G009 combined with stellar-synthesis models will allow its recent star formation history to be constrained and will provide a powerful check of this scenario. In particular, an intense starburst 100-300 Myr ago will be revealed through strong Balmer line absorption features resulting from the large numbers of A stars.

It must be noted, however, that even just the current line-of-sight velocity difference between ESO 349-G009 and ESO 349-G010/PKS2354-35 likely requires that ESO 349-G009 is marginally unbound to A 4059. Thus, if this galaxy is indeed the origin of the high metallicity plume, this system is a rare example of an unbound massive galaxy falling through the core of a rich cluster.

The temporal coincidence between the onset of powerful radio-galaxy activity and the hypothesized plunge/stripping of a large starburst galaxy suggests a connection. There are two principal possibilities. The close passage of a high velocity massive galaxy would tidally-shock any cold gas within the cD galaxy, driving an inflow and possibly triggering AGN activity. Alternatively, the gas stripped from the starburst galaxy is very likely to be multiphase (with regions of cold, atomic gas entrained by the hot X-ray emitting gas). Once stripped from the passing galaxy, the cold and dense atomic gas would preferentially fall (or, more precisely, sediment) into the cD galaxy and, again, possibly fuel the AGN activity. Either way, this presents a very different model of “radio-mode” AGN feedback to that normally envisaged; in this case, we are witnessing AGN feedback triggered directly by the close passage of a gas rich galaxy rather than radiative cooling of the host ICM.

We thank Steve Allen, Andrew Fabian, Stacy McGaugh, Richard Mushotzky David Rupke, and Kimberly Weaver for useful discussions. We also thank the anony-

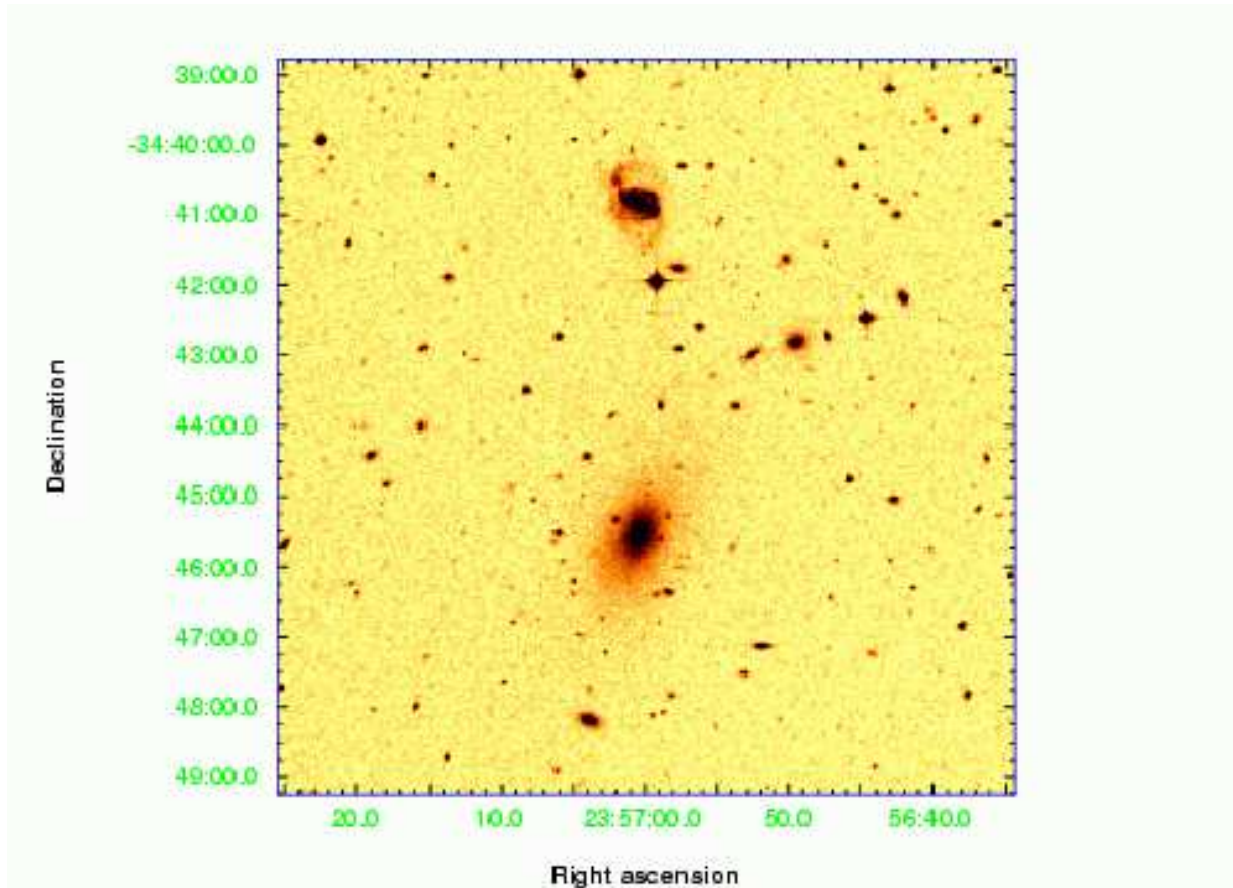


FIG. 10.— Digitized Sky Survey image of a 10×10 arcmin² field in the central regions of the A 4059 cluster. The cD galaxy ESO 349–G010 hosts the radio-galaxy PKS 2354–35 and resides at the center of the ICM atmosphere. The bright spiral galaxy ESO 349–G009 can be clearly seen to the north of the cD galaxy.

mous referee for insightful comments that significantly improved this paper. Finally, we are grateful to S. Diehl and T.S. Statler, whose WVT binning algorithm we utilized. This was a generalization of Cappellari & Copin’s

(2003) Voronoi binning algorithm. This work was supported by Smithsonian Astrophysical Observatory grant GO5-6128X.

REFERENCES

- Anders, E., Grevesse, N. 1989, *Geo Cosmo Acta*, 53, 197
 Baumgartner W.H., Loewenstein M., Horner D.J., Mushotzky R.F. 2005, *ApJ*, 620, 680
 Bell, E. F., McIntosh, D. H., Katz, N., & Weinberg, M. D. 2003, *ApJS*, 149, 289
 Benson, A. J., Bower, R. G., Frenk, C. S., Lacey, C. G., Baugh, C. M., & Cole, S. 2003, *ApJ*, 599, 38
 Blanton, E. L., Sarazin, C. L., McNamara, B. R., & Wise, M. W. 2001, *ApJ*, 558, L15
 Brüggén, M., & Kaiser, C. R. 2002, *Nature*, 418, 301
 Cappellari, M., & Copin, Y. 2003, *MNRAS*, 342, 345
 Choi, Y.-Y., Reynolds, C. S., Heinz, S., Rosenberg, J. L., Perlman, E. S., & Yang, J. 2004, *ApJ*, 606, 185
 Churazov, E., Forman, W., Jones, C., & Böhringer, H. 2003, *ApJ*, 590, 225
 Cowie, L. L., & Binney, J. 1977, *ApJ*, 215, 723
 de Vaucouleurs G., de Vaucouleurs A., Corwin Jr H.G., Buta R.J., Paturel G., Fouque, P. 1991, *Third Reference Catalogue of Bright galaxies*, Version 3.9
 Diehl, S., & Statler, T. S. 2006, *MNRAS*, 341
 Ettori, S., & Fabian, A. C. 2006, *MNRAS*, 369, L42
 Fabian, A. C., & Nulsen, P. E. J. 1977, *MNRAS*, 180, 479
 Fabian, A. C. 1994, *ARA&A*, 32, 277
 Fabian, A. C., et al. 2000, *MNRAS*, 318, L65
 Fabian, A. C. 2003, *MNRAS*, 344, L27
 Fabian, A. C., Sanders, J. S., Allen, S. W., Crawford, C. S., Iwasawa, K., Johnstone, R. M., Schmidt, R. W., & Taylor, G. B. 2003, *MNRAS*, 344, L43
 Fabian, A. C., Sanders, J. S., Taylor, G. B., & Allen, S. W. 2005, *MNRAS*, 360, L20
 Forman, W. et al. 2007, *ApJ*, 665, 1057
 Fujita Y., Sarazin C.L., Sivakoff, G.R. 2006, *PASJ*, 58, 131
 Gilfanov, M. R., Syunyaev, R. A., & Churazov, E. M. 1987, *Soviet Astronomy Letters*, 13, 3
 Heinz, S., Choi, Y.-Y., Reynolds, C. S., & Begelman, M. C. 2002, *ApJ*, 569, L79
 Heinz S., Churazov E., Forman W., Jones C., Briel U.G. 2003, *MNRAS*, 346, 13
 Holmberg, J., Flynn, C., & Portinari, L. 2006, *MNRAS*, 367, 449
 Huang, Z., & Sarazin, C. L. 1998, *ApJ*, 496, 728
 Johnstone, R. M., Allen, S. W., Fabian, A. C., & Sanders, J. S. 2002, *MNRAS*, 336, 299
 Jones, C., et al. 2004, 35th COSPAR Scientific Assembly, 4119
 Kaastra, J.S. 1992, *An X-Ray Spectral Code for Optically Thin Plasmas* (Internal SRON-Leiden Report, updated version 2.0)
 Kaiser, C. R. 2003, *MNRAS*, 343, 1319
 Liedahl, D. A., Osterheld, A. L., & Goldstein, W. H. 1995, *ApJ*, 438, L115
 Markevitch M. et al. 2000, *ApJ*, 541, 542
 Markevitch M. et al. 2002, *ApJ*, 567, L27.

- Matsushita, K., Belsole, E., Finoguenov, A., Böhringer, H. 2002, *A&A*, 386, 77
- McNamara, B. R., et al. 2000, *ApJ*, 534, L135
- McNamara, B. R., et al. 2001, *ApJ*, 562, L149
- Mewe, R., Gronenschild, E. H. B. M., & van den Oord, G. H. J. 1985, *A&AS*, 62, 197
- Mewe, R., Lemen, J. R., & van den Oord, G. H. J. 1986, *A&AS*, 65, 511
- Molendi, S. 2002, *ApJ*, 580, 815
- Nulsen, P. E. J., Hambrick, D. C., McNamara, B. R., Rafferty, D., Birzan, L., Wise, M. W., & David, L. P. 2005a, *ApJ*, 625, L9
- Nulsen, P. E. J., McNamara, B. R., Wise, M. W., & David, L. P. 2005b, *ApJ*, 628, 629
- Perlman, E. S., Stocke, J. T., Conway, J., & Reynolds, C.S. 2001, *AJ*, 122, 536
- Peterson, J. R., et al. 2001, *A&A*, 365, L104
- Peterson, J. R., & Fabian, A. C. 2006, *Phys. Rep.*, 427, 1
- Pizzolato, F., & Soker, N. 2005, *ApJ*, 632, 821
- Reverte D., Vichez J.M., Hernandez-Fernandez J.D., Iglesia-Paramo J. 2007, *AJ*, 133, 705
- Reynolds C.S., Heinz S., Begelman M.C., 2002, *MNRAS*, 332, 271
- Sanders, J. S., & Fabian, A. C. 2002, *MNRAS*, 331, 273
- Sanders, J. S., Fabian, A. C., Allen, S. W., & Schmidt, R. W. 2004, *MNRAS*, 349, 952
- Sanders, J. S., & Fabian, A. C. 2006, *MNRAS*, 370, 63
- Schmidt, R. W., Fabian, A. C., & Sanders, J. S. 2002, *MNRAS*, 337, 71
- Snowden S. et al. 2007, *ApJ*, in press
- Sun M., Jones, C., Forman, W., Vikhlinin A., Donahue M., Voit, M. 2007, *ApJ*, 657, 197
- Sutherland R.S., Dopita, M.A. 1993, *ApJS*, 80, 753
- Tamura, T., et al. 2001, *A&A*, 365, L87
- Taylor, G. B., Barton, E. J., & Ge, J. 1994, *AJ*, 107, 1942
- Vernaleo J.C., Reynolds, C.S. 2006, *ApJ*, 645, 83
- Vernaleo J.C., Reynolds, C.S. 2007, *ApJ*, 671, 171
- Wright, N. 2006, Ned Wright's Javascript Cosmology Calculator
- Young, A. J., Wilson, A. S., & Mundell, C. G. 2002, *ApJ*, 579, 560

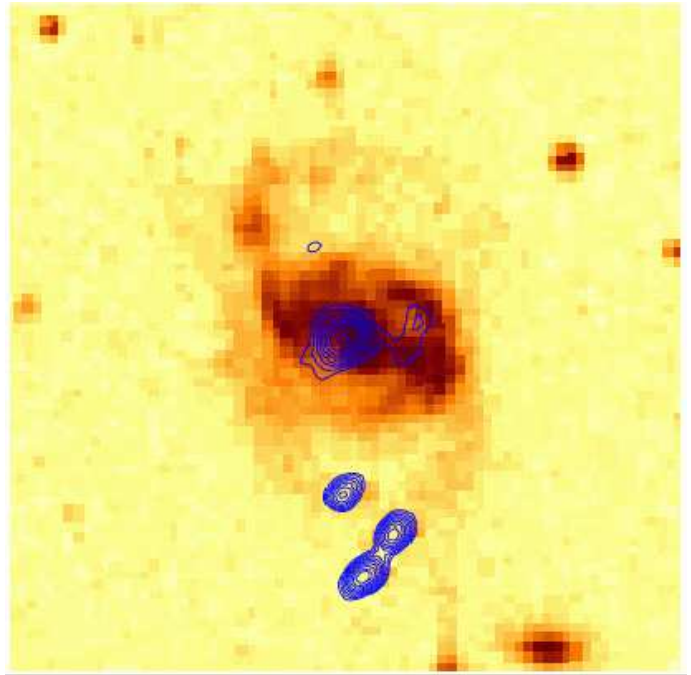


FIG. 11.— Digitized Sky Survey image of a 2×2 arcmin² field centered on ESO 349-G009. Overlaid are contours of the full-band (0.5–10 keV) X-ray intensity. See text and Sun et al. (2007) for a discussion of this emission.